Caractérisation de la Réponse Ultrasonore d'Implant Dentaire : Simulation Numérique et Analyse des Signaux

G Rosi, I Scala, V.H. Nguyen, Salah Naili, R Vayron, G Haiat, H Yahia, S Seuret, S Jaffard

CFA/VISHNO 2016

Caractérisation de la Réponse Ultrasonore d'Implant Dentaire : Simulation Numérique et Analyse des Signaux

G. Rosi[a], I. Scala[a], V.H. Nguyen[a], S. Naili[a], R. Vayron[a], G. Haiat[a], H. Yahia[b], S. Seuret[c] et S. Jaffard[c]

[a]Université Paris-Est, MSME UMR 8208 CNRS, 61, Avenue du Général de Gaulle, 94010 Créteil, France

[b]INRIA Bordeaux Sud-Ouest, 200 rue de la Vieille Tour, 33405 Talence, France

[c]Université Paris-Est, LAMA UMR 8050, UPEM, UPEC, CNRS, 61, Avenue du Général de Gaulle, 94010 Créteil, France

giuseppe.rosi@u-pec.fr

The long-term success of a dental implant is related to the properties of the bone-implant interface. It is important to follow the evolution of bone remodeling phenomena around the implant. To date, there is no satisfactory method for tracking physiological and mechanical properties of this area, and it is difficult for clinicians to qualitatively and quantitatively assess the stability of a dental implant. In this context, methods based on ultrasound wave propagation were already successfully used by our group, in the qualitative and quantitative evaluation of primary and secondary stability of dental implants. In this study we perform numerical simulations, using the finite element method, of wave propagation in a dental implant inserted into bone. To simplify the calculations, an axisymmetric geometry is considered. Given the importance of monitoring of peri-prosthetic area, particular attention is given to the boundary conditions between the implant and the bone. The numerical results are compared with those from experimental tests. These results, numerical and experimental, are then analysed with signal processing tools based on multifractal methods. Analysis of the first results shows that these methods are potentially efficient in this case because they can explore and exploit the multi-scale structure of the signal.

1 Introduction

The development of acoustical modeling and of the associated numerical simulation are mandatory in order to understand the interaction between an ultrasonic wave and the bone–implant system because it can help improving the performances of the device under development. Moreover, using modelling approaches is the only solution in order to discriminate the effects of the different bone parameters (such as bone structure, geometry and material properties) on the ultrasonic response of the implant, which is nearly impossible to achieve *in vivo* because all parameters vary in parallel.

This study highlights the potentiality of quantitative ultrasound techniques to study dental implant stability because it gives more insight on the ultrasonic propagation in the bone–implant system [1, 2]. Future work should focus on considering other dental implant geometries and developing more accurate modeling of osseointegration phenomena, thus leading to a more realistic description of the medical device under development. Another perspective consists in solving the inverse problem given by the determination of the implant stability based on its ultrasonic response.

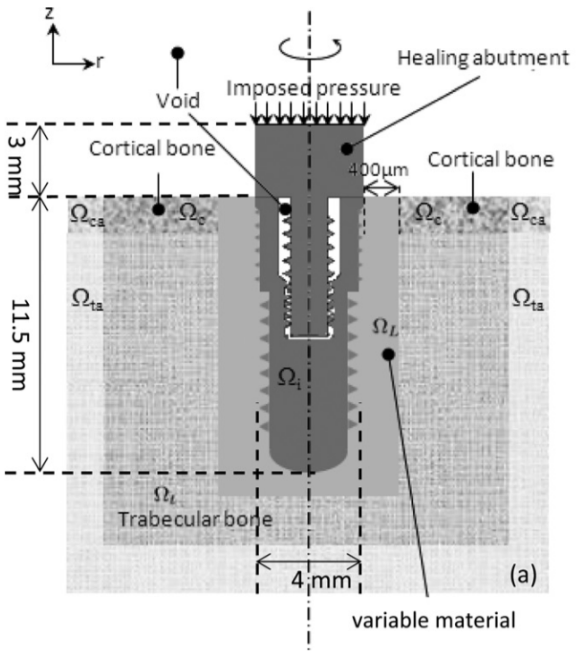

Figure 1: Cross-section view of the 3-D axisymmetric geometrical configuration used in the numerical simulations (image extracted from [4]).

2 Finite Element Analysis

Due to the symmetry with respect to the implant's axis of the system and boundary conditions, an axisymmetric assumption was considered. The experimental device uses a contact planar 10MHz transducer positioned at the emerging surface of the implant [1].

The geometrical configuration used in the simulation is shown in Fig. 1. The bone sample is modeled as a bi-layer structure which consists of a 1 mm thick layer of cortical bone Ω_c and a trabecular bone halfspace Ω_t. The geometry of the titanium dental implant Ω_i (length L=11.5 mm and diameter D =4 mm) represents a dental implant commercialised by Implants Diffusion International (IDI1240, IDI, Montreuil, France). A specific healing abutment (IDI, Montreuil, France) was used and was screwed on the top of the dental implant. The healing abutment is inserted into the implant to avoid tissue formation inside the implant. The implant is completely buried in the bone sample, this configuration modelling the clinical configuration. The region Ω_L is the peri-prosthetic layer, and it is defined by the domain located between the implant surface and mature bone tissue, and containing either bone tissue or water depending on the configuration. All media considered in this model are assumed to have homogeneous isotropic mechanical properties, and volume forces are neglected.

The axial symmetric equations of motion are:

$$\rho\ddot{u}_r - \frac{\partial\sigma_{rr}}{\partial r} - \frac{1}{r}\frac{\partial\sigma_{rz}}{\partial z} - \frac{\sigma_{rr}-\sigma_{\theta\theta}}{r} = 0, \quad (1)$$

$$\rho\ddot{u}_z - \frac{\partial\sigma_{zz}}{\partial z} - \frac{\sigma_{rz}}{r} = 0, \quad (2)$$

where ρ is the mass density; u_r and u_z are the radial and axial components of the displacement vector; σ_{rr}, σ_{rz}, $\sigma_{\theta\theta}$, σ_{zz} are the components of the stress tensor denoted by σ and the double superimposed dot stands for a second partial dime derivative. The constitutive relation using Hooke's laws is given by:

$$\sigma = \lambda tr(\boldsymbol{\varepsilon})\mathbb{I} + \mu\boldsymbol{\varepsilon} \quad (3)$$

where λ, μ denote the Lamé constants, $tr()$ the trace of a tensor, $\mathbb{I}$ is the identity tensor and $\boldsymbol{\varepsilon}$ is the strain tensor whose nonzero components are given by:

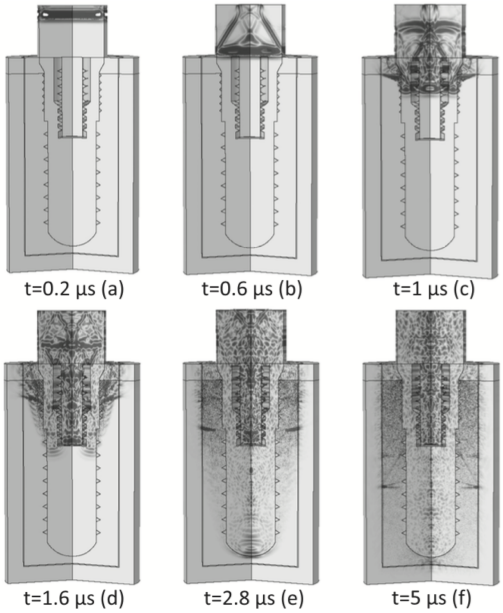

Figure 2: Cartography of amplitude of V_z (geometrical configuration of the Fig. 1) at six different times after the emission [(a) 0.2, (b) 0.6, (c) 1, (d) 1.6, (e) 2.8, and (f) 5 μs] (image extracted from [4]).

$$\varepsilon_{rr} = \frac{\partial u_r}{\partial r}, \quad \varepsilon_{\theta\theta} = \frac{u_r}{r}, \quad \varepsilon_{rz} = \frac{1}{2}\left(\frac{\partial u_r}{\partial z} + \frac{\partial u_z}{\partial z}\right), \tag{4}$$

$$\varepsilon_{zz} = \frac{\partial u_z}{\partial z}. \tag{5}$$

The emitted signal from the planar ultrasonic contact transducer is modelled as a time pulse uniform pressure applied on the top surface of the implant. Here, a time-dependent function defined by

$$p(t) = Ae^{-4(f_c t-1)^2}\sin(2\pi f_c t), \tag{6}$$

where A is an amplitude, f_c is the central frequency of the pulse and t denotes the time. The discretization of the equations leads to a transient linear dynamic problem. The full description of the finite element problem can be found in [3]. The output radio frequency (rf) signal was determined by computing the spatial average of the pressure at the upper surface of the implant. Extracting informations form a complex signal obtained from the ultrasonic probe is a challenging task. Indeed, the first approach used in [1, 2] is based on the analysis of the envelope of the signal. To verify if the numerical simulations are in agreement with experiments, the same signal processing technique as the one employed in [1] was used to derive a quantitative indicator I based on the envelope of the transient signal:

$$I = \sum_{i=1}^{N} S(it_0) \tag{7}$$

where N is the number of samples, t_0 the sampling rate, and $S(t)$ the envelope of the signal.

As an example, the synthetic signal recorded in the numerical tests is plotted in Fig. 3. The computation of the aforementioned indicator I is plotted in Fig. 4. As it can be seen, the numerical results are in agreement with experiments. However, since the measured signal is the result of multiple reflections occurring also at the interface between the bone and the implant, we do expect that more informations could be extracted from a multi-scale analysis.

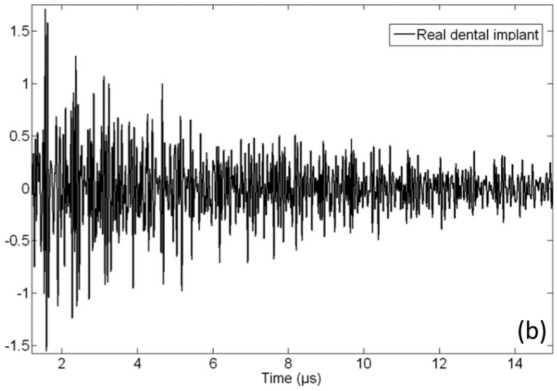

Figure 3: Numerical signal obtained from the sensor (image extracted from [4]).

3 Signal processing and multifractal analysis

With the aim of extracting more information from the complex output signal, we applied multifractal techniques to both experimental and numerical data.

Multifractal analysis aims at describing both the scaling properties of a signal and the distribution of its local singularities. The notion of "multifractal signal" was used with success in turbulence to find a formula relating the "quantity" of singularities of a given order of the signal with some structure function (which is a global quantity computed on the signal). The main interest of this formula is that, although the singularities of a signal are very complicated to localize and to estimate, the structure function is directly computable with various methods (based on increments, wavelets or Fourier transform), and the algorithms involved are relatively fast for signals of reasonable size. So the multifractal approach allows one to access to the intern structure of signals. In this framework, multifractal tools have been used to analyse the various scaling invariance

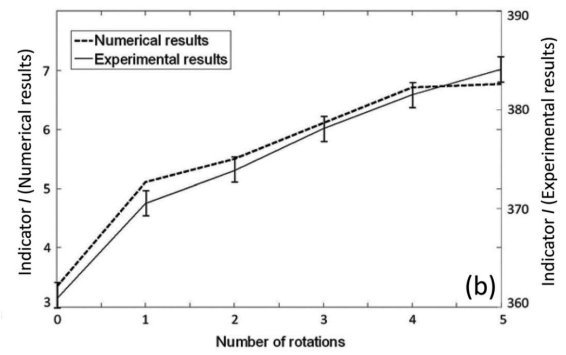

Figure 4: Variation of the simulated (dashed lines) and experimental (solid lines) indicator I as a function of the number of unscrewing rotation of the dental implant in bone tissue (image extracted from [4]).

properties of both the synthetic and real signals under consideration. One can hope to exhibit relevant parameters characterising the composition and/or the microstructural properties of the bone-implant (for instance, self-similar properties).

3.1 Wavelet bases

Orthonormal wavelet bases on the real set $\mathbb{R}$ are of the following form: There exists two functions $\varphi(x)$ and $\psi(x)$ such that the functions $\varphi(x-k)$, $k \in \mathbb{Z}$, and $2^{j/2}\psi(2^j x - k)$, $k \in \mathbb{Z}$, where $\mathbb{Z}$ is the set of integers, $j \geq 0$, form an orthonormal wavelet basis of $L^2(\mathbb{R})$, the space of squared integrable functions. This basis is called "r-smooth" if φ and ψ are in the space of r-times differentiable continuous functions C^r and if the derivatives $\varphi^{(\alpha)}$, and $\psi^{(\alpha)}$, for $|\alpha| \leq r$, have fast decay. This requirement implies that, for any polynomial P of degree less than r,

$$\int_{\mathbb{R}} P(x)\psi(x)dx = 0. \tag{8}$$

The orthonormal basis condition means that $\forall f \in L^2(\mathbb{R})$,

$$f(x) = \sum_{k\in\mathbb{Z}} c_k \varphi(x-k) + \sum_{j=0}^{\infty}\sum_{k\in\mathbb{Z}} c_{j,k}\psi(2^j x - k), \tag{9}$$

where the $c_{j,k}$ and c_k are called the *wavelet coefficients* of f and given by

$$c_{j,k} = 2^j \int_{\mathbb{R}} f(x)\psi(2^j x - k)dx, \tag{10}$$

$$c_k = \int_{\mathbb{R}} f(x)\varphi(x-k)dx. \tag{11}$$

Note that the computation of the coefficients given by (10) and (11) makes sense with very little assumption on f (a wide mathematical setting is supplied by tempered distributions, if the wavelets belong to the Schwartz class: The integrals have then to be understood as duality products in the sense of distributions).

We will use more compact notations for indexing wavelets:

- Instead of using the indices (j,k), we will use dyadic intervals

$$\lambda\,(=\lambda(j,k)) \;= \left[\frac{k}{2^j}, \frac{k+1}{2^j}\right),$$

and, accordingly: $c_\lambda = c_{j,k}$ and $\psi_\lambda(x) = \psi(2^j x - k)$. Indexing by dyadic intervals will be useful in the sequel because the interval λ indicates the localization of the corresponding wavelet. Note that the wavelet ψ_λ is essentially localized near λ.

- Λ_j will denote the set of dyadic interval λ which index a wavelet of scale j, *i.e.*, wavelets of the form $\psi_\lambda(x) = \psi(2^j x - k)$.

3.2 The wavelet structure function

The *wavelet structure function* of f is

$$S_f(p,j) = 2^{-j}\sum_{\lambda\in\Lambda_j} |c_\lambda|^p. \tag{12}$$

Its order of magnitude in the limit of small scales can be related with the Sobolev regularity of the data as follows. Let us define the *wavelet scaling function* by

$$\forall p \geq 1, \qquad \eta_f(p) = \liminf_{j\to+\infty} \frac{\log\left(S_f(p,j)\right)}{\log(2^{-j})}. \tag{13}$$

The definition supplied by (13) yields the scaling function through linear regressions in log-log plots.

Let $p \geq 1$ and $s \in \mathbb{R}$; a tempered distribution f belongs to $L^{p,s}(\mathbb{R}^d)$ if its Fourier transform $\hat{f}$ is a function satisfying the following property: If $\hat{g}(\xi) = (1+|\xi|^2)^{s/2}\hat{f}(\xi)$, then $g \in L^p$. The different variants in the definition of Sobolev spaces and the embeddings between them imply that

$$\eta_f(p) = p\,\sup\left\{\, s : \quad f \in L^{p,s}_{loc}\,\right\}. \tag{14}$$

Note that this result only holds if the wavelets used are smooth enough. The rule of thumb is that wavelets should be smoother and have more vanishing moments than the regularity index appearing in the definition of the function space. In the following we will never specify the required smoothness, and always assume that *smooth enough wavelets* are used (the minimal regularity required being always easy to infer).

4 Numerical results

A first multifractal analysis, based on the wavelet coefficients [7, 8], shows that signals obtained from simulations and experiments have a specific particular multifractal signature. This means the log-log regressions on the multi-scale exponents could be used for a classification of the different configurations of interest. The relation (13) is used when the log-log plot regression of the wavelet structure function as the function of the scale yields a straight line. In Fig. 5 we plotted two examples of $\log\left(S_f(p,j)\right)$ as a function of $-j$. The curves have been computed using the Wavelet Leader and Bootstrap based MultiFractal analysis (WLBMF) toolbox, [5, 6]. First of all, this figure shows that there is no scale invariance, so that only keeping an average slope would be too reductive. On the opposite, we believe that introducing classification tools on the whole graph would be pertinent. Indeed, from the comparison between 5(a) and 5(b), we can observe that the multifractal signature for two experimental configurations enough different is relatively identical. This permanent feature points out

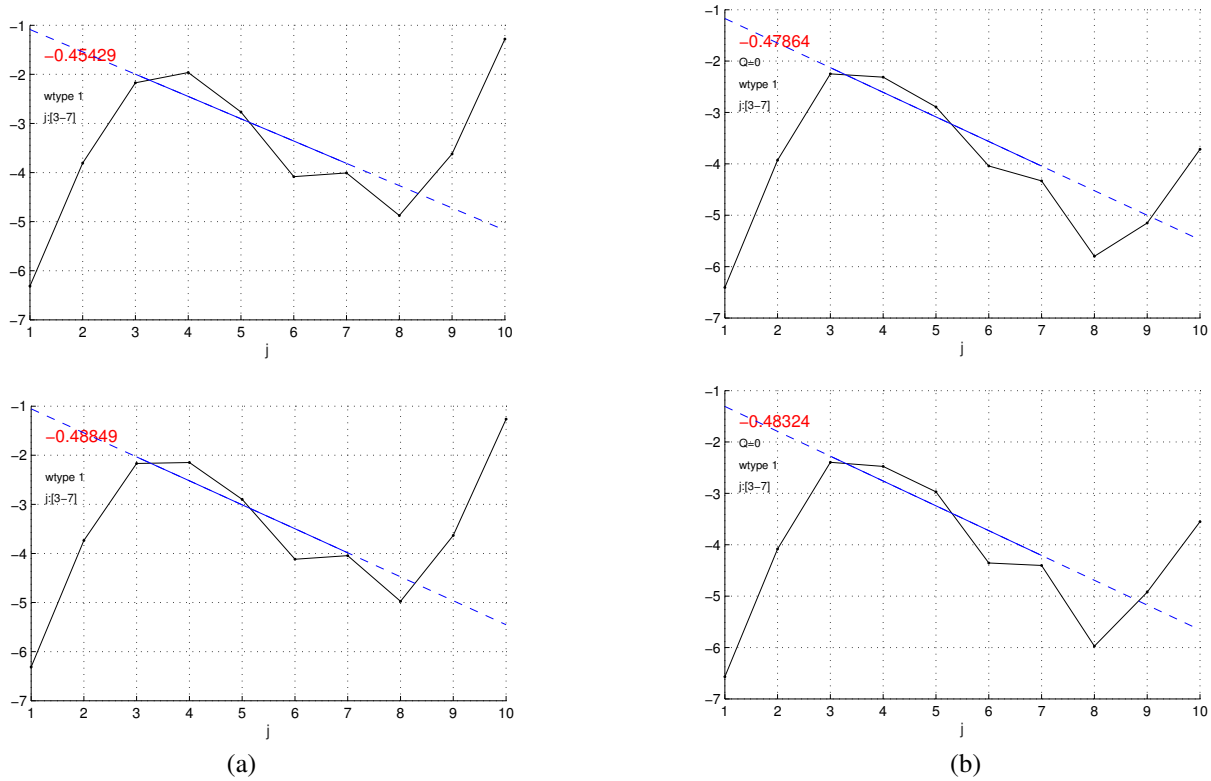

Figure 5: Example of log-log plots of the wavelet structure function for $p = 1 : \log_2\left(S_f(p, j)\right)$ *versus* $-j$. The analysis is performed on experimental data obtained from two different specimens for two different stability conditions: (a) implant fully inserted in the bone, (b) implant half unscrewed and immersed into water.

that we must get the information from the shape of these curves. As a consequence, their classification, for a large amount of numerical and experimental data, will be the object of a further study. This study will be focused on the process of inspecting data, whose goal is discovering useful information and suggesting conclusions by classifying the signals from the shape of the wavelet structure function, as done in [9].

Acknowledgements

This work was supported by French National Research Agency (ANR) through the PRTS program (project OsseoWave ANR-13-PRTS-0015 and by the Université Paris-Est through the PEPS program (15R03051A-METCARMAT).

References

[1] R. Vayron, P. Karasinski, V. Mathieu, A. Michel, D. Loriot, G. Richard, G. Lambert, and G. Haïat, *Variation of the ultrasonic response of a dental implant embedded in tricalcium silicate-based cement under cyclic loading*, Journal of Biomechanics, **46**(6), 1162–1168 (2013).

[2] R. Vayron, V. Mathieu, A. Michel, and G. Haïat, *Assessment of in vitro dental implant primary stability using an ultrasonic method*, Ultrasound in Medicine and Biology **40**(12), 2885–2894, (2014).

[3] R. Vayron, V. -H. Nguyen, R. Bosc, S. Naili, and G. Haïat, *Finite element simulation of ultrasonic wave propagation in a dental implant for biomechanical stability assessment*, Biomechanical Models in Mechanobiology, **14**(5), 1021–1032, (2015).

[4] R. Vayron, V. -H. Nguyen, R. Bosc, S. Naili, and G. Haïat, *Assessment of the biomechanical stability of a dental implant with quantitative ultrasound: A three-dimensional finite element study,* Journal of the Acoustical Society of America, **139**(2), 773–780, (2016).

[5] H. Wendt, P. Abry, S. Jaffard, *Bootstrap for Empirical Multifractal Analysis*, IEEE Signal Processing Magazine, **24**(4), 38-48, (2007).

[6] H. Wendt, S. G. Roux, P. Abry, S. Jaffard, *Wavelet leaders and bootstrap for multifractal analysis of images*, Signal Processing, **89**, 1100-1114, (2009).

[7] P. Abry, S. Jaffard, H. Wendt, *Irregularities and Scaling in Signal and Image Processing: Multifractal Analysis*, Benoit Mandelbrot: A Life in Many Dimensions, M. Frame and N. Cohen, Eds., World scientific publishing, 31–116, (2015).

[8] P. Abry, S. Jaffard, H. Wendt, *A bridge between geometric measure theory and signal processing: Multifractal analysis*, Operator-Related Function Theory and Time-Frequency Analysis, The Abel Symposium 2012, K. Gröchenig, Y. Lyubarskii and K. Seip, Eds., Springer, **9**, 1-56, (2015).

[9] P. Abry, S. G. Roux, H. Wendt, P. Messier, A. G. Klein, N. Tremblay, P. Borgnat, S. Jaffard, B. Vedel, J. Coddington, L. Daffner, *Multiscale Anisotropic Texture Analysis and Classification of Photographic Prints: Art scholarship meets image processing algorithms*, IEEE Signal Processing Magazine, **32**(4), 18-527, (2015).